Verification methods for one-dimensional particle-in-cell/Monte Carlo collisional simulations

Jón Tómas Guðmundsson[1,2]

[1] Space and Plasma Physics, KTH Royal Institute of Technology, Stockholm, Sweden
[2] Science Institute, University of Iceland, Reykjavik, Iceland
tumi@hi.is

77th Gaseous Electronics Conference
San Diego, California
September 30., 2024

Introduction

- The particle-in-cell Monte Carlo collsion simulations are frequently used to illustrate physical mechanisms in low-temperature plasmas
- The particle in cell algorithm approximates the distribution function with a set of computational particles that are evolved in time according to Newton's laws
- The electric and magnetic fields acting on the particles are computed self consistently by solving the Maxwell's equations
- Their basic formulations is conceptually very simple
- Thanks to PIC/MCC simulations, significant progress has been made in the understanding of fundamental plasma phenomena

Introduction

- With improved models it is becoming possible to make quantitative predictions for real applications
- This makes it is even more urgent to apply:
  - **Verification**: A comparison of simulations and analytical solutions to test the intrinsic consistency of a model
  - **Validation**: A comparison of simulations with experimental results or observations
  - **Benchmarking**: A comparison of two or more models under the same conditions, but with different numerical implementations or on different scales (like particle or fluid models)

Ute Ebert et al., Plasma Sources Science and Technology, Special Issue on Verification, Validation and Benchmarking of Low-temperature Plasma Models

Introduction

The American Society of Mechanical Engineers (ASME) Guide defines verification as:

- Verification: the process of determining that a computational model accurately represents the underlying mathematical model and its solution

and code verification as

- Code verification: the process of determining that the numerical algorithms are correctly implemented in the computer code and of identifying errors in the software

Oberkampf and Roy (2010), Verification and Validation in Scientific Computing, Cambridge University Press

Introduction

Code verification usually involves:

- performing simple tests (e.g., energy conservation tests)
- comparing simulation results with results from other codes (also known as code-to-code benchmark)
- quantifying the numerical error with respect to the exact solution
- testing the convergence of the numerical solution to the exact solution
- comparing the rate of convergence of the numerical solution to the expected order of the numerical scheme (order-of-accuracy tests)

Riva et al. (2017) *Physics of Plasmas*, **24**(5) 055703

Validation: `XPDP1` in argon

performing simple tests

Validation: XPDP1 *in argon*

Plasma Sources Sci. Technol. 2(1993) 273–278. Printed in the UK

Capacitive RF discharges modelled by particle-in-cell Monte Carlo simulation. II: comparisons with laboratory measurements of electron energy distribution functions

V Vahedi†, C K Birdsall†, M A Lieberman†, G DiPeso‡ and T D Rognlien‡

†Department of Electrical Engineering and Computer Science, University of California, Berkeley, CA 94720, USA
‡Lawrence Livermore National Laboratory, Livermore, CA 94550, USA

Received 25 February 1993, in final form 11 July 1993

Abstract. Bi-Maxwellian electron energy distribution functions (EEDFs) have been measured experimentally in argon RF discharges at 13.56 MHz by Godyak *et al* (*Plasma Sources Sci. Technol.* 1 36 (1992)). The observed EEDFs at low pressures had very-low-energy and high-energy components. We show particle-in-cell Monte-Carlo (PIC-MCC) simulations, which produce the same EEDFs. Excellent agreement is obtained between the effective low and high electron temperatures in simulations and those measured in the laboratory. Our simulations, with the same physical parameters as in the laboratory, obtain the same transition point in the electron heating mode, from stochastically dominated heating at low pressures to ohmically dominated heating at high pressures.

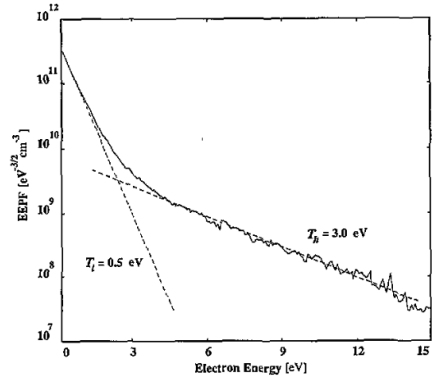

Figure 2. The EEPF obtained from a current-driven argon RF discharge simulation driven at 13.56 MHz with a discharge current of 2.56 mA cm^{-2} in a 2 cm gap, at a neutral pressure of 100 mTorr. The broken lines represent the two-temperature Maxwellian distribution of the discharge.

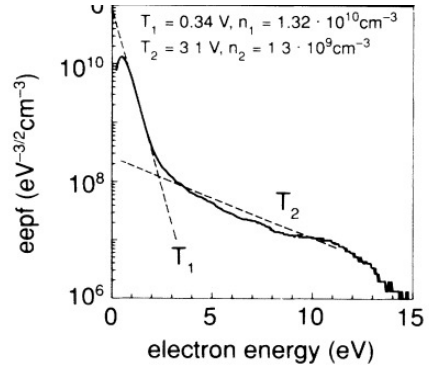

FIG. 2. The EEPF (lower) and normalized EEDF (upper) $F(\varepsilon)/n_0$, obtained for p =0.1 Torr and I_d =0.3 A rms.

- An early version of XPDP1 was validated against measurements of the electron energy distribution and plasma parameters in a capacitive argon discharge

Vahedi et al. (1993) PSST **2** 273

Godyak and Piejak (1990) PRL **65**(8) 996

Validation: XPDP1 *in argon*

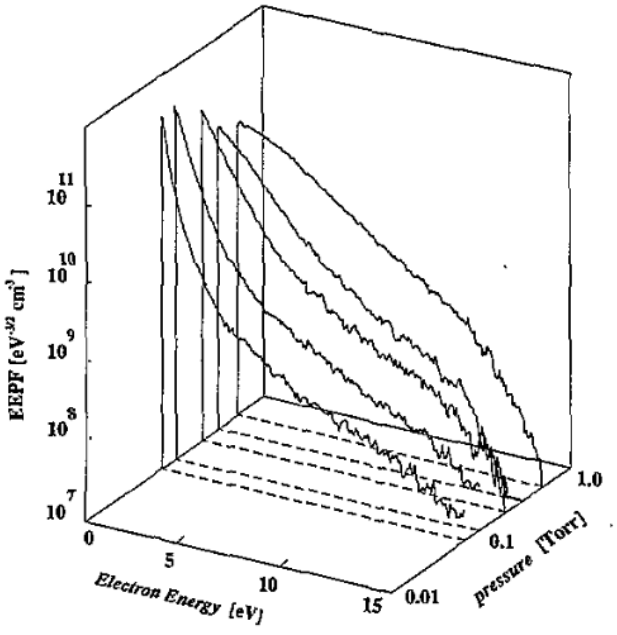

Figure 3. The EEPFs from a current-driven argon RF discharge simulation running at 13.56 MHz with a 2 cm gap over a range of pressures.

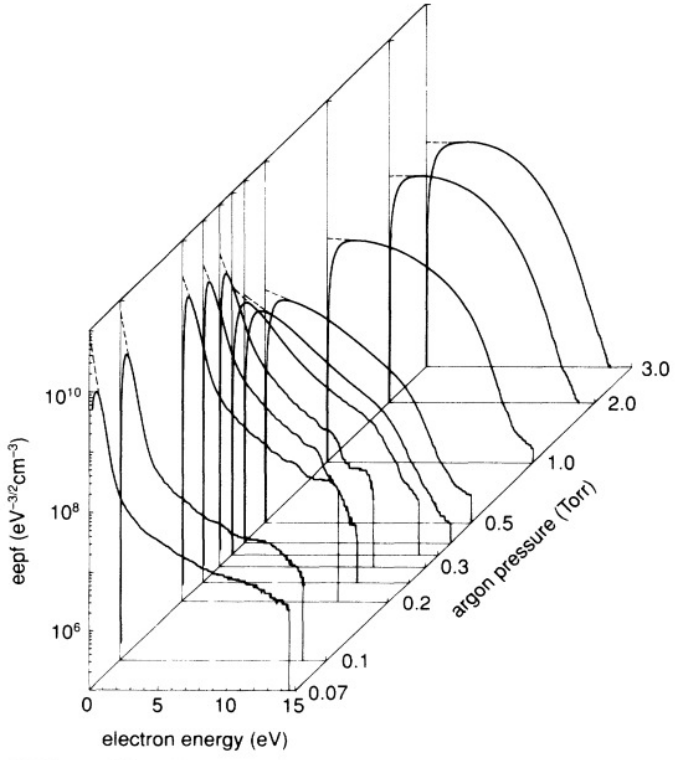

FIG. 3. The EEPF evolution with changing argon pressure, I_d =0.3 A rms.

Vahedi et al. (1993) PSST **2** 273

Godyak and Piejak (1990) PRL **65**(8) 996

- The electron energy probability function (EEPF)

Validation: XPDP1 *in argon*

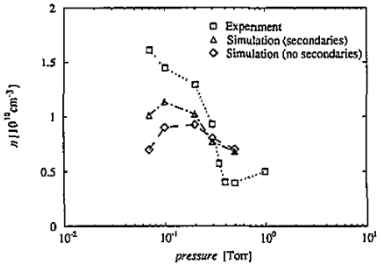

Figure 5. Average plasma density measured in the middle of the system in a 2 cm gap current-driven argon RF at 13.56 MHz. The squares are measurements by Godyak *et al* [4]; the diamonds are simulation results without secondary electron emission; the triangles are simulation results with secondary electron emission.

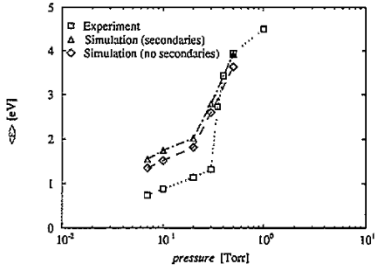

Figure 7. Average electron energy in the system in a 2 cm gap current-driven argon RF discharge. Same symbols as in figure 5.

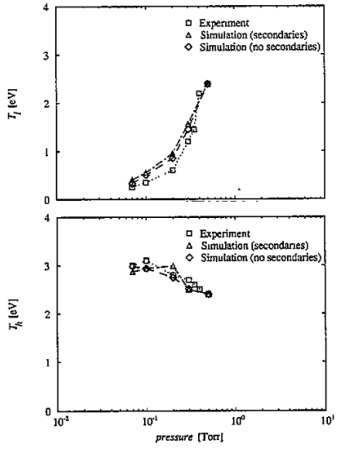

Figure 6. Comparison of effective temperatures of low- and high-energy electron groups in the system in a 2 cm gap current-driven argon RF discharge. Same symbols as in figure 5.

Vahedi et al. (1993) PSST **2** 273

- The plasma densities, measured in the center of the discharge gap and those measured by Godyak et al.
- Two sets of simulation results are shown, with and without secondary electron emission due to ion impact ($Y_\mathrm{i} = 0.2$)
- Even with secondaries, the plasma density from the simulation is still roughly a factor of two lower

Validation: `XPDP1` *in argon*

- Vahedi et al. obtained smaller electron density and larger electron temperature in their simulation than those in the measurement by roughly a factor of two
- Using larger number of superparticles for the same number of cells Kim et al. find the electron density and electron temperature to be in better agreement with those in Godyak's measurement under low pressure

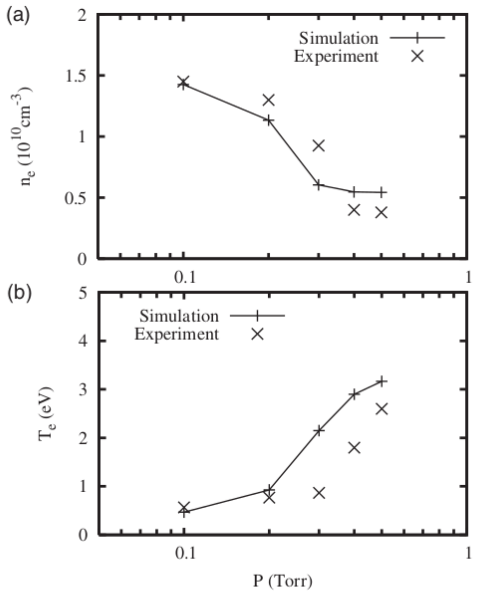

Fig. 2. (a) Electron densities and (b) electron temperatures at the discharge center as a function of gas pressure. The calculated values in our simulations are compared with the measured ones in Godyak's experiments.[3)]

Kim et al. (2005) JJAP **44**(4A) 1957

Godyak and Piejak (1990) PRL **65**(8) 996

Validation: PHOENIX1D *in argon*

- Similarly Lafleur et al. validated the code PHOENIX1D against measurements of the electron density and energy in a capacitive argon discharge
- The densities from the simulations are slightly lower, while the electron energies are slightly higher than the measured values
- They used the same or larger number of superparticles than Kim et al.

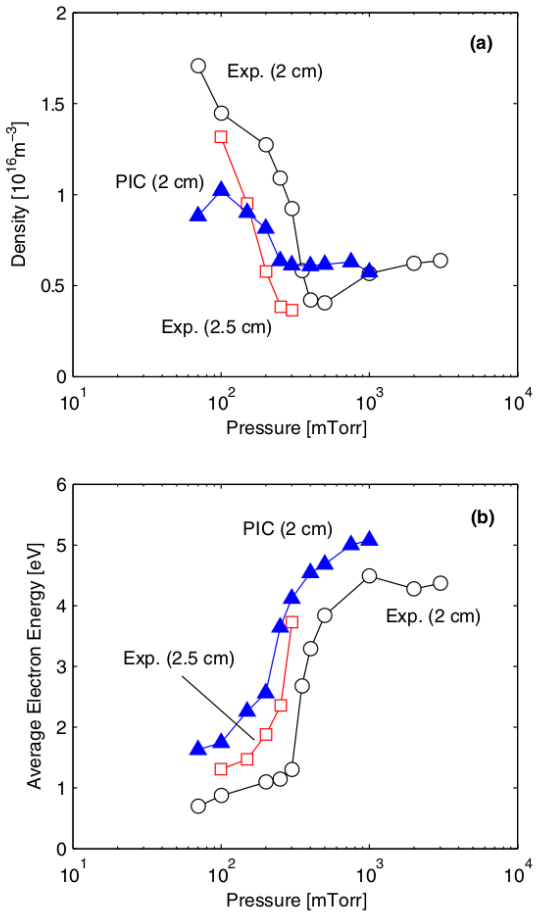

Figure 2. (*a*) Central plasma density, and (*b*) average electron energy as a function of argon gas pressure. The open black circles show experimental results with a gap length of 2 cm taken from [4], while the open red squares are experimental results with a gap length of 2.5 cm taken in the DRACULA reactor described in section 4. Closed blue triangles show the PIC simulation results.

Lafleur et al. (2014) PSST **23**(3) 035010

Godyak and Piejak (1990) PRL **65**(8) 996

Code-to-code Benchmark

`OOPD1` vs `XPDP1`

comparing simulation results with results from other codes

Code-to-code Benchmark

- Another common, or the usual approach, to verify particle-in-cell simulation codes and evaluate the error affecting a simulation result is based on performing code-to-code comparisons

Surendra (1995) PSST **4**(1) 56

Turner et al. (2013) Physics of Plasmas **20**(1) 013507

Gudmundsson et al. (2013) PSST **22** 035011

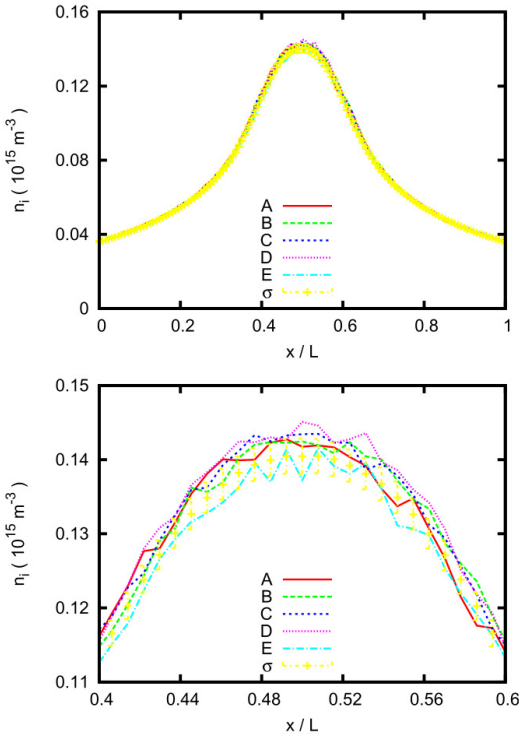

FIG. 7. Ion density distribution for case 1. The curves labelled A to E show the results obtained by the indicated code. The points with error bars show the standard deviation obtained from an extended calculation using code E.

Turner et al. (2013) Phys. Plasmas **20**(1) 013507

The oopd1 1d-3v PIC/MCC code

- We use the `OOPD1` (objective oriented plasma device for one dimension) code to simulate the discharge
- The `OOPD1` code was originally developed at the Plasma Theory and Simulation Group at UC Berkeley
- It has 1 dimension in space and 3 velocity components for particles (1d-3v)
- The `OOPD1` code is supposed to replace the widely used `XPDX1` series (`XPDP1`, `XPDC1` and `XPDS1`)
- It is developed to simulate various types of plasmas, including processing discharges, accelerators and beams
  - Modular structure
  - Includes relativistic kinematics
  - Particles can have different weights

Gudmundsson et al. (2013) *Plasma Sources Sci. Technol.*, **22**(3) 035011

Wen et al. (2021) *Plasma Sources Sci. Technol.*, **30**(10) 105009

Code-to-code Benchmark: `OOPD1` *vs* `XPDP1`

- We performed a benchmark study and compared the `OOPD1` code to the well-established planar `XPDP1` code
- The cross section set in `XPDP1` is limited to O_2^+, O^- and electrons as the charged particles
- We compared
  - the electron energy distribution function
  - the electron temperature profile
  - the density profiles of charged particles
  - electron heating rates

  for a 4.5 cm gap capacitive oxygen discharge at 50 mTorr

Case	Code	Cross section set	Electron kinematics
1	xpdp1	xpdp1	xpdp1
2	oopd1	xpdp1	xpdp1
3	oopd1	xpdp1	oopd1
4	oopd1	oopd1 limited	oopd1
5	oopd1	oopd1 full	oopd1

Gudmundsson et al. (2013) PSST **22** 035011

Code-to-code Benchmark: `OOPD1` *vs* `XPDP1`

Reaction	Process	In xpdp1	Reference
Electron-impact O_2			
$e + O_2 \longrightarrow O_2 + e$	Elastic scattering	x	[21]
$e + O_2(r = 0) \longrightarrow e + O_2(r > 0)$	Rotational excitation	x	[25]
$e + O_2(v = 0) \longrightarrow e + O_2(v > 0)$	Vibrational excitation	x	[25]
$e + O_2 \longrightarrow e + O_2(a\,^1\Delta_g)$	Metastable excitation (0.98 V)	x	[25]
$e + O_2 \longrightarrow e + O_2(b\,^1\Sigma_g^+)$	Metastable excitation (1.63 V)	x	[25]
$e + O_2 \longrightarrow e + O_2(A\,^3\Sigma_u^+, A'\,^3\Delta_u, c\,^1\Sigma_u^-)$	Metastable excitation (4.05 V)	x	[21–23]
$e + O_2 \longrightarrow O(^3P) + O(^3P) + e$	Dissociation (6.12 V)	x	[25]
$e + O_2 \longrightarrow O(^3P) + O(^1D) + e$	Dissociation (8.4 V)	x	[25]
$e + O_2 \longrightarrow O(^1D) + O(^1D) + e$	Dissociation (9.97 V)	x	[25]
$e + O_2 \longrightarrow O_2^+ + 2e$	Electron-impact ionization (12.06 V)	x	[26]
$e + O_2 \longrightarrow e + O + O(3p^3P)$	Dissociative excitation (14.7 V)	x	[25]
$e + O_2 \longrightarrow O + O^-$	Dissociative attachment	x	[27]
$e + O_2 \longrightarrow O^+ + O^- + e$	Polar dissociation		[27]
$e + O_2 \longrightarrow O^+ + O + 2e$	Dissociative ionization		[26]
Electron-impact O			
$e + O \longrightarrow O + e$	Elastic scattering		[29, 30]
$e + O(^3P) \longrightarrow O(^1D) + e$	Excitation to ^1D (1.96 eV)		[31]
$e + O(^3P) \longrightarrow O(^1S) + e$	Excitation to ^1S (4.18 eV)		[31]
$e + O(^3P) \longrightarrow O(^3P^0) + e$	Excitation to $^3P^0$ (15.65 eV)		[31]
$e + O(^3P) \longrightarrow O(^5S^0) + e$	Excitation to $^5S^0$ (9.14 eV)		[31]
$e + O(^3P) \longrightarrow O(^3S^0) + e$	Excitation to $^3S^0$ (9.51 eV)		[31]
$e + O \longrightarrow O^+ + 2e$	Ionization (13.62 eV)		[32]
Detachment			
$e + O^- \longrightarrow O + 2e$	Electron-impact detachment	x	[39]
$O^- + O_2 \longrightarrow O + O_2 + e$	Detachment by oxygen molecule	x	[40]
$O^- + O \longrightarrow O_2 + e$	Detachment by oxygen atom		[41]
Recombination			
$e + O_2^+ \longrightarrow O(^3P) + O(^1D)$	Dissociative recombination	x	[33, 34]
$O^- + O_2^+ \longrightarrow O + O_2$	Mutual neutralization	x	[37, 36]
$O^+ + O^- \longrightarrow O + O$	Mutual neutralization		[37, 38]
Charge exchange			
$O_2^+ + O_2 \longrightarrow O_2 + O_2^+$	Charge exchange	x	[42–44]
$O^+ + O_2 \longrightarrow O + O_2^+$	Charge exchange		[46]
$O^+ + O \longrightarrow O + O^+$	Charge exchange		[47]
$O_2^+ + O \longrightarrow O_2 + O^+$	Charge exchange (1.56 eV)		[48, 51]
$O_2^+ + O_2 \longrightarrow O^+ + O + O_2$	Fragmentation by energetic O_2^+		See text
Scattering			
$O^- + O_2 \longrightarrow O^- + O_2$	Scattering	x	[49]
$O + O_2 \longrightarrow O + O_2$	Scattering	x	[45]
$O_2^+ + O_2 \longrightarrow O_2^+ + O_2$	Scattering	x	See text
$O^+ + O_2 \longrightarrow O^+ + O_2$	Scattering		See text
$O_2 + O_2 \longrightarrow O_2 + O_2$	Scattering		[45]
$O + O \longrightarrow O + O$	Scattering		See text

Gudmundsson et al. (2013) PSST **22** 035011

Code-to-code Benchmark: OOPD1 *vs* XPDP1

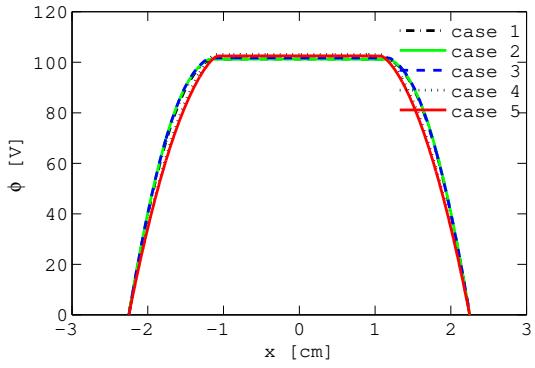

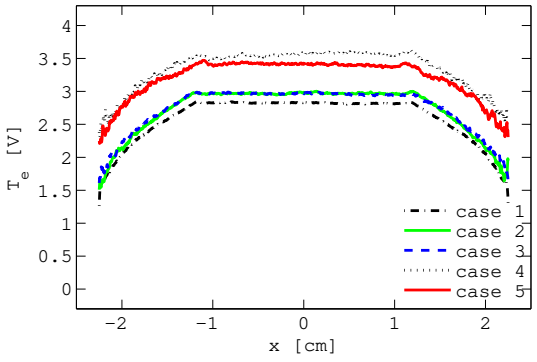

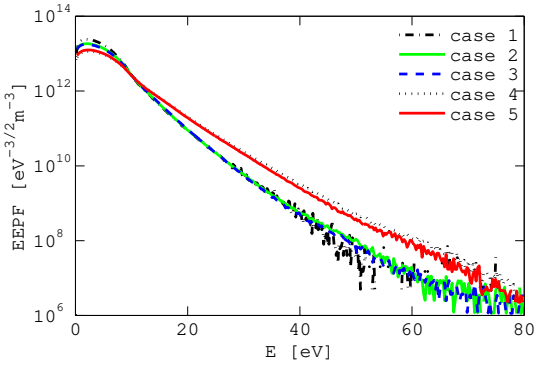

- The electron energy probability function (EEPF) is almost the same when the XPDP1 cross sections are used
- There is a slightly higher density of low-energy electrons when the XPDP1 code is used (case 1) than when the OOPD1 code is used
- This explains the lower effective electron temperature observed when using XPDP1

Case	Code	Cross section set	Electron kinematics
1	xpdp1	xpdp1	xpdp1
2	oopd1	xpdp1	xpdp1
3	oopd1	xpdp1	oopd1
4	oopd1	oopd1 limited	oopd1
5	oopd1	oopd1 full	oopd1

Gudmundsson et al. (2013) PSST **22** 035011

Code-to-code Benchmark: OOPD1 *vs* XPDP1

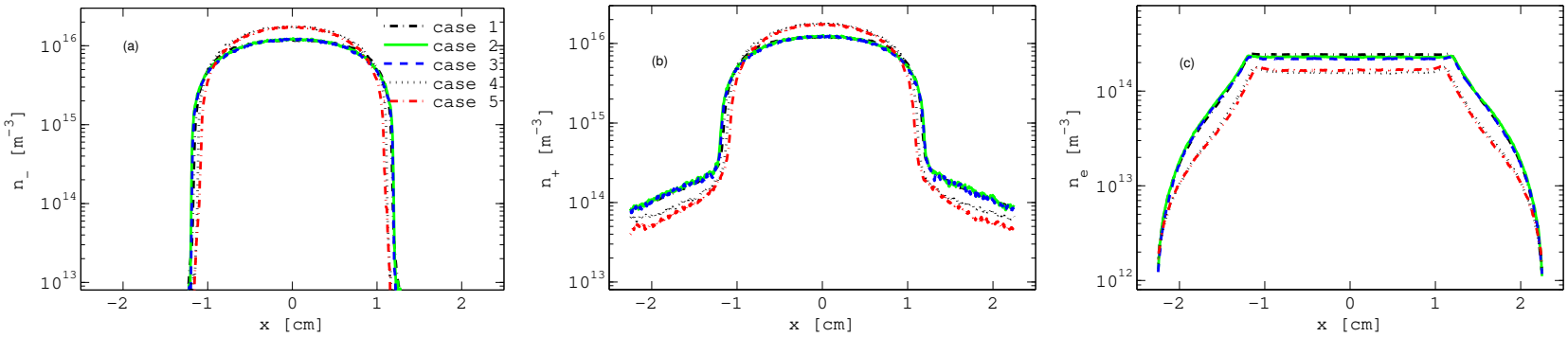

- The density profiles for O^- ions, O_2^+ ions and electrons
- The negative ion profile is almost the same for both XPDP1 and OOPD1 using the XPDP1 cross sections
- With the limited revised cross section set, case 4, the negative ion density profile is slightly narrower and the peak density at the discharge center is higher

Case	Code	Cross section set	Electron kinematics
1	xpdp1	xpdp1	xpdp1
2	oopd1	xpdp1	xpdp1
3	oopd1	xpdp1	oopd1
4	oopd1	oopd1 limited	oopd1
5	oopd1	oopd1 full	oopd1

Gudmundsson et al. (2013) PSST **22** 035011

Code-to-code Benchmark: OOPD1 *vs* XPDP1

- The electron heating rate profile
- The peaks near the plasma-sheath boundaries are mainly due to pressure heating and the electron power absorption in the bulk is primarily due to ohmic heating of slow electrons
- The enhanced treatment of the collision kinematics in OOPD1 leads to an increase in the ohmic heating and decrease in the pressure heating
- The revised cross section set further increases the ohmic heating in the bulk plasma and decreases the pressure heating

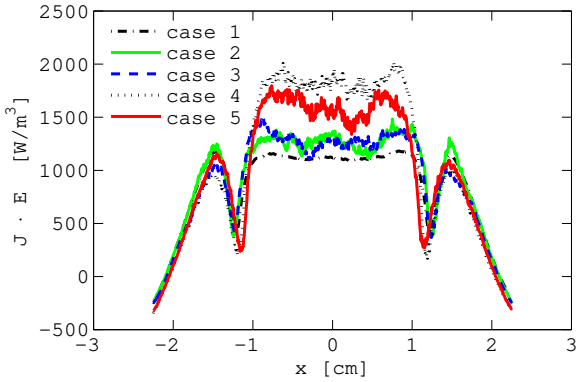

Case	Code	Cross section set	Electron kinematics
1	xpdp1	xpdp1	xpdp1
2	oopd1	xpdp1	xpdp1
3	oopd1	xpdp1	oopd1
4	oopd1	oopd1 limited	oopd1
5	oopd1	oopd1 full	oopd1

Gudmundsson et al. (2013) PSST **22** 035011

Code-to-code Benchmark: OOPD1 *vs* XPDP1

- The previous figure of the power absorption at 50 mTorr in oxygen is incorrect
- Detachment by the metastable molecule $O_2(a^1\Delta_g)$ has a significant influence on the discharge properties such as the electronegativity, the effective electron temperature and the electron power absorption processes
  - **Case 1** – the complete reaction set
  - **Case 2** – detachment by $O_2(a^1\Delta_g)$ neglected
  - **Case 5** – no metastables, the benchmark
  - **Case 6** – complete reaction set with $\gamma_{i,see} = 0.2$

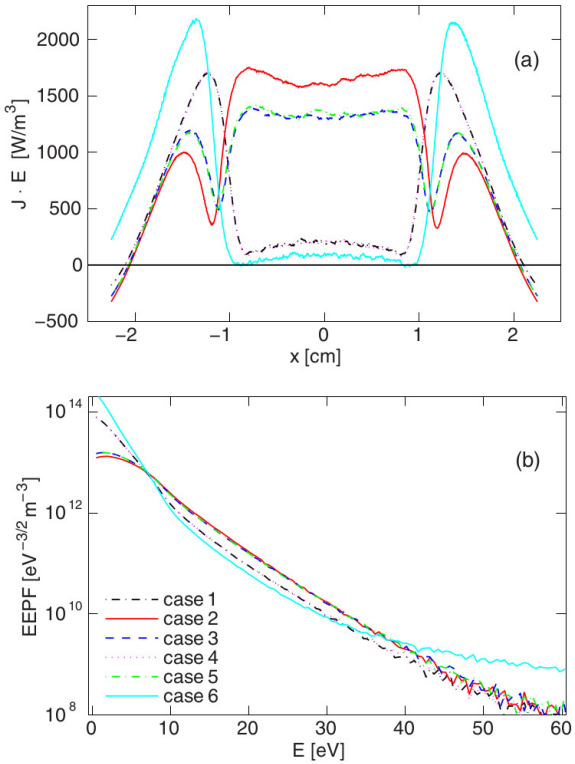

Figure 6. The (a) electron heating rate profile and the (b) electron energy probability function (EEPF) in the discharge center for a parallel plate capacitively coupled oxygen discharge at 50 mTorr with a gap separation of 4.5 cm by a 222 V voltage source at 13.56 MHz.

Code verification

quantifying the numerical error with respect to the exact solution

testing the convergence of the numerical solution to the exact solution

comparing the rate of convergence of the numerical solution to the expected order of the numerical scheme (order-of-accuracy tests)

Code verification

- PIC codes are used to numerically solve the Vlasov-Maxwell system of equations
- The PIC algorithm represents the distribution function of plasma species as a set of computational particles (superparticles), whose position in the phase space is evolved according to Newton's laws
- The forces acting on the particles are obtained by solving the Maxwell equations, having assigned to a numerical grid the charge and the current carried by the particles

Code verification

- The model we consider is written

$$\frac{\partial f_\alpha}{\partial t} + v\frac{\partial f_\alpha}{\partial x} + \frac{q_\alpha E}{m_\alpha}\frac{\partial f_\alpha}{\partial v} = 0 \quad \textit{and} \quad \frac{\partial E}{\partial x} = \frac{\rho}{\epsilon_0}$$

  where $f_\alpha(x, v, t)$ is the distribution function for the species α, ρ is the total charge distribution and E is the electric field
- In the PIC method these equations are solved numerically performing the following steps:
  - At $t = 0$, N_p superparticles are randomly distributed in the phase space according to a distribution function f_0 and a weight w_p is assigned to each particle

$$w_p = \frac{f(x_p, v_p, t = 0)}{f_0(x_p, v_p)}$$

Code verification

- The particle charge is assigned to a numerical grid with spacing Δx, to obtain the charge distribution at each grid point
- The Poisson equation is solved and the electric field E is computed on the grid
- E is interpolated from the grid to the particle positions, to obtain the electric field E_p acting on each particle
- The equations of motion of the computational particles

$$\frac{\mathrm{d}w_p}{\mathrm{d}t} = 0, \quad \frac{\mathrm{d}x_p}{\mathrm{d}t} = v_p, \quad \frac{\mathrm{d}v_p}{\mathrm{d}t} = \frac{q}{m} E_p$$

  are numerically integrated in time to $t = \Delta t$, with Δt being the step of the time integration scheme

- The system is advanced until the final time of the simulation is reached

Code verification

- The error associated with a statistical representation of the distribution function is expected to decrease as

$$\frac{1}{\sqrt{N_p}}$$

where N_p is a measure of the number of simulation particles

- The numerical error affecting quantities such as E_p, that result from a simulation is

$$\epsilon = C_1 \Delta x^b + C_2 \Delta t^b + C_3 \frac{1}{\sqrt{N_p}} + \text{higher order terms}$$

where C_1, C_2 and C_3 are constants

  - a is the order of accuracy of the spatial operators in the interpolation between particles and grid positions
  - b is the order of accuracy of the time integration scheme

Code verification

- To simplify the expression of the numerical error, it is useful to introduce
  - p the theoretical order of accuracy of the algorithm
  - h representing the degree of refinement of the mesh and time step
- Then

$$h^p = \left(\frac{\Delta x}{\Delta x_0}\right)^a + \left(\frac{\Delta t}{\Delta t_0}\right)^b + \left(\frac{N}{N_0}\right)^{-1/2}$$

  and consequently

$$\epsilon_h = C_p h^p + \mathcal{O}(h^{p+1})$$

- Often $p = a$ the theoretical order of accuracy of the algorithm is taken as the order of accuracy of the spatial discretization scheme

Code verification

- For a kinetic model M solved by a PIC code, we denote its exact solution as s

$$M(s) = 0$$

  and its numerical discretization with degree of refinement h as M_h
- The numerical solution of M_h is denoted as s_h

$$M_h(s_h) = 0$$

- The numerical error affecting the simulation results is defined as

$$\epsilon = \|s - s_h\|$$

  where $\|\cdot\|$ denotes a designated norm
- The evaluation of the numerical error ϵ_h requires that s is known

Analytical verification solution

quantifying the numerical error with respect to the exact solution

Analytical verification solution

IOP Publishing
Plasma Sources Science and Technology
Plasma Sources Sci. Technol. **31** (2022) 114008 (16pp)
https://doi.org/10.1088/1361-6595/aca1db

Space-charge affected current flow: an analytical verification solution for kinetic and fluid simulation models

T Lafleur

ThrustMe, Verrières-le-Buisson F-91370, France

- There are not many true analytical solutions for kinetic simulations due to the complexity of the Vlasov and Boltzmann equations
- One such solution is the space-charge limited (SCL) charged particle flow through a planar diode
- This solution has been used to verify several electrostatic PIC simulation codes
- The particles are assumed to be injected cold and collisions with any background gas are neglected

Analytical verification solution

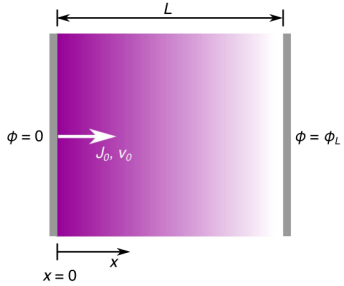

Figure 1. Charged particle flow between two parallel plate electrodes.

Lafleur (2020) PSST **29**(6) 065002

- Lafleur extended this work by deriving a complete solution valid for any injection current from zero up until the SCL limit

  Lafleur (2022) PSST **31**(11) 114008
- The system consists of two parallel electrodes separated by a distance L
- At the left-hand side electrode ($x = 0$), charged particles of only one sign are injected and subsequently accelerated towards the right-hand side electrode (at $x = L$)
- The initial particle injection velocity is v_0 and the injected current density is J_0

Analytical verification solution

- The analytical equations in Tables 1 and 2 serve as useful verification solutions to demonstrate the correctness and accuracy of numerical simulations, such as PIC codes
- The parameter

$$\beta = \sqrt{-\frac{mv_0^2}{2q\phi_L}}$$

effectively represents the initial particle energy relative to the total accelerating potential

Table 1. Solution below the transition current density ($0 \leqslant J_0 \leqslant J_{\rm tr}$) with parameters β and μ (and where $0 \leqslant \mu < \infty$).

Variable	Analytical solution
Transition current	$\frac{J_{\rm tr}}{J_{\rm CL}} = \frac{q}{\lvert q\rvert}\left[\sqrt{\sqrt{\beta^2+1}-\beta}\left(\sqrt{\beta^2+1}+2\beta\right)\right]^2$ where $\beta = \sqrt{-\frac{mv_0^2}{2q\phi_L}}$ and $J_{CL} = \frac{4\epsilon_0}{9}\sqrt{\frac{2\lvert q\rvert}{m}}\frac{\lvert\phi_L\rvert^{3/2}}{L^2}$
Normalized current	$\alpha = \frac{2}{3}\left[\sqrt{\sqrt{\beta^2+1}-\beta+\mu}\left(\sqrt{\beta^2+1}+2\beta-2\mu\right)-\sqrt{\mu}\,(3\beta-2\mu)\right]$ where $0 \leqslant \mu < \infty$
Injection current	$\frac{J_0}{J_{\rm CL}} = \frac{q}{\lvert q\rvert}\frac{9\alpha^2}{4}$
Potential	$\frac{2}{3\alpha}\left[\sqrt{\sqrt{\beta^2+\frac{\phi(x)}{\phi_L}}-\beta+\mu}\left(\sqrt{\beta^2+\frac{\phi(x)}{\phi_L}}+2\beta-2\mu\right)-\sqrt{\mu}\,(3\beta-2\mu)\right] = \frac{x}{L}$
Electric field	$\frac{E(x)}{E_L} = -2\alpha\sqrt{\sqrt{\beta^2+\frac{\phi(x)}{\phi_L}}-\beta+\mu}$ where $E_L = \frac{\phi_L}{L}$
Density	$\frac{n(x)}{n_L} = \frac{1}{\sqrt{\beta^2+\frac{\phi(x)}{\phi_L}}}$ where $n_L = \frac{J_0}{qv_L}$
Velocity	$\frac{v(x)}{v_L} = \sqrt{\beta^2+\frac{\phi(x)}{\phi_L}}$ where $v_L = \sqrt{-\frac{q\phi_L}{m}}$

Table 2. Solution above the transition current density ($J_{\rm tr} < J_0 \leqslant J_{\rm scl}$) with parameters β and η^* (and where $\frac{\beta\sqrt{\beta^2+1}}{\beta+\sqrt{\beta^2+1}} \leqslant \eta^* < \beta$).

Variable	Analytical solution
Transition current	$\frac{J_{\rm tr}}{J_{\rm CL}} = \frac{q}{\lvert q\rvert}\left[\sqrt{\sqrt{\beta^2+1}-\beta}\left(\sqrt{\beta^2+1}+2\beta\right)\right]^2$ where $\beta = \sqrt{-\frac{mv_0^2}{2q\phi_L}}$ and $J_{CL} = \frac{4\epsilon_0}{9}\sqrt{\frac{2\lvert q\rvert}{m}}\frac{\lvert\phi_L\rvert^{3/2}}{L^2}$
Space-charge limited current	$\frac{J_{\rm scl}}{J_{\rm CL}} = \frac{q}{\lvert q\rvert}\left(\beta+\sqrt{\beta^2+1}\right)^3$
Normalized current	$\alpha = \frac{2}{3}\left[\sqrt{\sqrt{\beta^2+1}-\eta^*}\left(\sqrt{\beta^2+1}+2\eta^*\right)+\sqrt{\beta-\eta^*}\,(\beta+2\eta^*)\right]$ where $\frac{\beta\sqrt{\beta^2+1}}{\beta+\sqrt{\beta^2+1}} \leqslant \eta^* < \beta$
Injection current	$\frac{J_0}{J_{\rm CL}} = \frac{q}{\lvert q\rvert}\frac{9\alpha^2}{4}$
Stationary point	$\frac{x^*}{L} = \frac{2}{3\alpha}\sqrt{\beta-\eta^*}\,(\beta+2\eta^*)$
Potential	$\left[\frac{x^*}{L}-\frac{2}{3\alpha}\sqrt{\sqrt{\beta^2+\frac{\phi(x)}{\phi_L}}-\eta^*}\left(\sqrt{\beta^2+\frac{\phi(x)}{\phi_L}}+2\eta^*\right)\right] = \frac{x}{L}$ for $(\eta^{*2}-\beta^2) \leqslant \frac{\phi(x)}{\phi_L} \leqslant 0$ and $0 \leqslant x \leqslant x^*$
Potential	$\left[\frac{x^*}{L}+\frac{2}{3\alpha}\sqrt{\sqrt{\beta^2+\frac{\phi(x)}{\phi_L}}-\eta^*}\left(\sqrt{\beta^2+\frac{\phi(x)}{\phi_L}}+2\eta^*\right)\right] = \frac{x}{L}$ for $(\eta^{*2}-\beta^2) < \frac{\phi(x)}{\phi_L} \leqslant 1$ and $x^* < x \leqslant L$
Electric field	$\frac{E(x)}{E_L} = 2\alpha\sqrt{\sqrt{\beta^2+\frac{\phi(x)}{\phi_L}}-\eta^*}$ for $0 \leqslant x \leqslant x^*$ and where $E_L = \frac{\phi_L}{L}$
Electric field	$\frac{E(x)}{E_L} = -2\alpha\sqrt{\sqrt{\beta^2+\frac{\phi(x)}{\phi_L}}-\eta^*}$ for $x^* < x \leqslant L$
Density	$\frac{n(x)}{n_L} = \frac{1}{\sqrt{\beta^2+\frac{\phi(x)}{\phi_L}}}$ where $n_L = \frac{J_0}{qv_L}$
Velocity	$\frac{v(x)}{v_L} = \sqrt{\beta^2+\frac{\phi(x)}{\phi_L}}$ where $v_L = \sqrt{-\frac{q\phi_L}{m}}$

Analytical verification solution

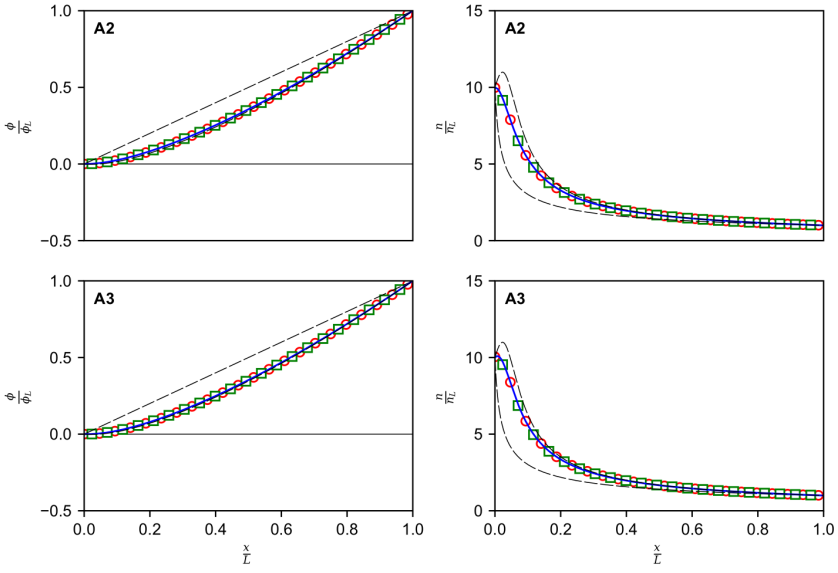

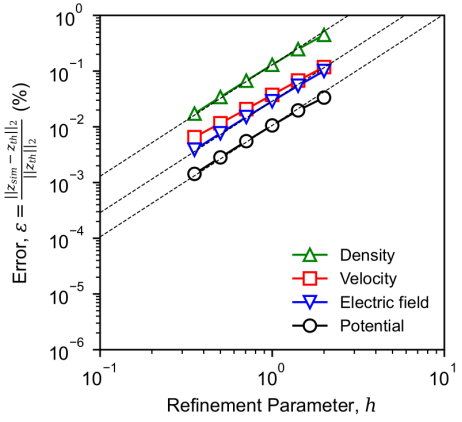

Figure 7. Relative L2 vector norm solution error as a function of the refinement parameter with the PIC simulations for verification case A2. The black dashed lines show a reference second-order theoretical convergence rate.

- Spatial profiles of the potential (left column) and density (right column) for verification cases with $\beta = 0.1$
- The solid blue curves show the theoretical results, the open red circles the PIC simulation results, and the open green squares the fluid simulation results
- The dashed black lines show theoretical results at injection current densities equal to zero and at the SCL limit respectively

Analytical verification solution

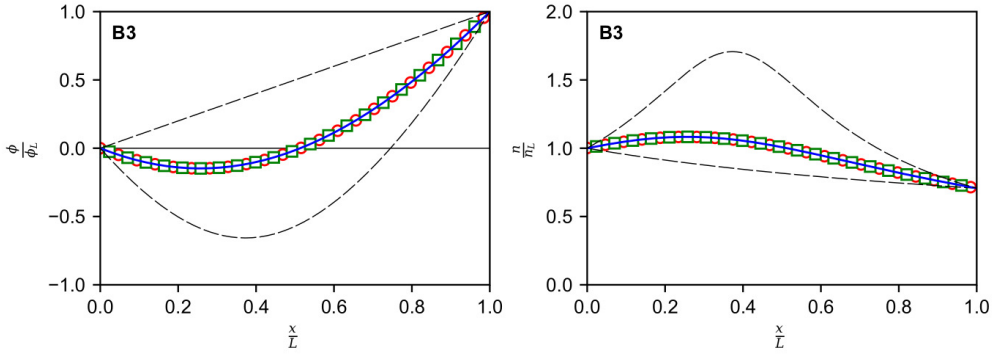

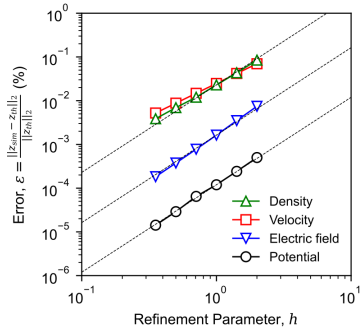

Figure 8. Relative L2 vector norm solution error as a function of the refinement parameter with the PIC simulations for verification case B3. The black dashed lines show a reference second-order theoretical convergence rate.

- Spatial profiles of the potential (left column) and density (right column) for verification cases with $\beta = 1$
- The solid blue curves show the theoretical results, the open red circles the PIC simulation results, and the open green squares the fluid simulation results
- The dashed black lines show theoretical results at injection current densities equal to zero and at the SCL limit respectively

Lafleur (2022) PSST **31**(11) 114008

Analytical verification solution

- The numerical errors can be explicitly quantified
- Recall that

$$\epsilon = C_1 \Delta x^b + C_2 \Delta t^b + C_3 \frac{1}{\sqrt{N_p}} \quad \textit{and} \quad \epsilon_h = C_p h^p$$

  where

$$h^p = \left(\frac{\Delta x}{\Delta x_0} \right)^a + \left(\frac{\Delta t}{\Delta t_0} \right)^b + \left(\frac{N_p}{N_0} \right)^{-1/2}$$

- By simultaneously refining the numerical parameters Δx, Δt and N_p, an overall convergence rate of order p can in principle be obtained

Analytical verification solution

- In the PIC simulations, the leap-frog time integration scheme is second-order so that $b = 2$
- Similarly, the electrostatic field solver is second-order in space while linear weighting is used for particle-grid/grid-particle interpolation, so $a = 2$
- For a target convergence rate of order $p = 2$

$$h = \left(\frac{\Delta x}{\Delta x_0}\right) + \left(\frac{\Delta t}{\Delta t_0}\right) + \left(\frac{N_p}{N_0}\right)^{-1/4}$$

- Halving the refinement parameter doubles the number of time steps, but the number of particles required increases by a factor of 16

Analytical verification solution

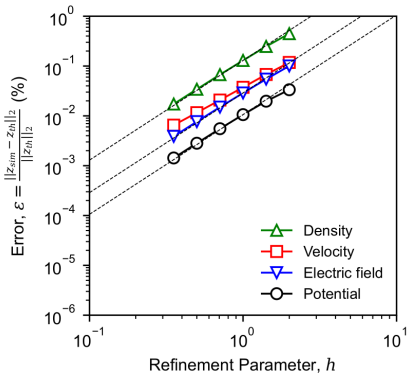

Figure 7. Relative L2 vector norm solution error as a function of the refinement parameter with the PIC simulations for verification case A2. The black dashed lines show a reference second-order theoretical convergence rate.

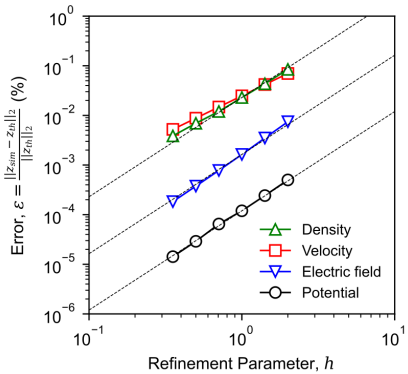

Figure 8. Relative L2 vector norm solution error as a function of the refinement parameter with the PIC simulations for verification case B3. The black dashed lines show a reference second-order theoretical convergence rate.

- The error is

$$\epsilon = \frac{\left\| z_{\text{sim}} - z_{\text{theo}} \right\|_2}{\left\| z_{\text{theo}} \right\|_2}$$

  and z is certain spatial quantity and

$$\|z\|_2 = \sqrt{\sum_{i=1}^{N} z_i^2}$$

- As the refinement parameter is reduced the solution converges and the error continuously decreases

Method of manufactured solutions (MMS)

Method of manufactured solutions (MMS)

- There are not many true analytical solutions for kinetic simulations due to the complexity of the Vlasov and Boltzmann equations – the solution s is unknown in most cases
- The MMS was developed to overcome this issue
- Instead of solving M analytically, an arbitrary function s_M is imposed as a solution to the model (the manufactured solution)
- The model equations are modified to accommodate the imposed solution; the modified model is then solved numerically to compute the numerical error
- For a given model M, we choose an analytical function s_M and compute a source term, $S = M(s_M)$, which is subsequently subtracted from M to obtain a new analytical model G

$$G = M - S$$

Method of manufactured solutions (MMS)

- The analytical solution of G is s_M

$$G(s_M) = M(s_M) - S = 0$$

and

$$G_h = M_h - S = 0$$

which can be solved numerically to obtain $s_{M,h}$

- Since the source term S is computed analytically, we do not add any new source of numerical error to the original numerical model, and the numerical error

$$\epsilon_h = \|s_M - s_{M,h}\|$$

satisfies

$$\epsilon_h = C' h^p + \mathcal{O}(h^{p+1})$$

where C' is a constant independent of h

Method of manufactured solutions (MMS)

- The manufactured solution should satisfy the following requirements
  - be sufficiently smooth and not singular
  - satisfy the code constraints (e.g., $f \geq 0$ and $f \to 0$ for $v \to \pm\infty$
  - be general enough to excite all terms present in the equations
  - ensure that the different terms composing the equations are of the same order of magnitude so that no term dominates the others
- The manufactured solutions are usually built as a combination of trigonometric and/or hyperbolic functions

Riva et al. (2017) *Physics of Plasmas*, **24**(5) 055703

Tranquilli et al. (2022) *Journal of Computational Physics*, **448** 110751

Method of manufactured solutions (MMS)

- Verification using the method of manufactured solutions is based on solving numerically a new, arranged system that is related to the original system, and for which we know the exact solution
- Verification is performed via the comparison of a theoretical convergence rate to the exact solution with an empirically measured convergence rate
- If these convergence rates match, then we know both that the implemented numerical process is converging to the correct solution and that it matches the intended underlying algorithm

Method of manufactured solutions (MMS)

- The new system of equations to be solved is simply the previous Vlasov-Poisson equation with the addition of a specific forcing term

$$S_f(x, v, t) = \frac{\partial f_M}{\partial t} + v\frac{\partial f_M}{\partial x} + \frac{qE_M}{m}\frac{\partial f_M}{\partial v}$$

and

$$S_E(x, t) = \frac{\partial E_M}{\partial x} - \frac{\rho}{\epsilon_0}$$

with $S_E = 0$ if E_M is consistent with f_M

- Here f_M and E_M are the desired manufactured solution, and solve exactly the modified system


Method of manufactured solutions (MMS)

- The addition of a source term in the Vlasov equation requires a small modification to the particle-in-cell procedure – the equation of motion for the particle weight now has a nonzero right-hand side

$$\frac{\mathrm{d}w_p}{\mathrm{d}t} = \frac{S_f(x_p(t), v_p(t), t)}{f_0(x_p(0), v_p(0))}$$

- The task is then to compute the numerical error affecting the simulation results
- For the electric field it involves finding the difference between the numerical and the manufactured solution as

$$\epsilon(E_p) = \max_t \max_{p=1,\ldots,N} |E_p(t) - E_M(x_p(t), t))|$$

Method of manufactured solutions (MMS)

- To quantify the numerical error affecting f_M requires measurement of the distance between a continuous analytical distribution function and a set of N_p computational particles
- The evaluation of $\epsilon_p(f_M)$ is computationally expensive for a data set with a large number of elements
- Challenges associated with comparing simulation results, which consist of discrete particle distributions, with the continuous analytical distributions of the manufactured solution – computationally expensive

Method of manufactured solutions (MMS)

- Note that deriving the manufactured solution typically requires the underlying equations and physical model to be modified
  - the introduction of additional source terms
  - new differential equations (such as an equation for the evolution of the particle weight)
- This may mean changes to the simulation code which creates an addition burden on the simulator, and can introduce new errors
- The manufactured solutions typically describe artificial or physically unobtainable systems, and therfore may provide limited insight into any actual underlying physics

Lafleur (2022) PSST **31**(11) 114008

Validation: OOPD1 in argon

Including metastable states and surface effects

Pressure dependence – no surface effects

Pressure dependence

- The ionization rate profiles at
  - 50 mTorr (upper)
  - 1.6 Torr (lower)
  - rf current source at 50 $\mathrm{A/m^2}$
- The results show varying completeness of the discharge model
- The blue line indicates simulations where the metastable $\mathrm{Ar^m}$, the radiative $\mathrm{Ar^r}$, and the Ar(4p) manifold are included and modeled as time- and space-evolving fluid species
- Without excited species there is no ionization in the bulk

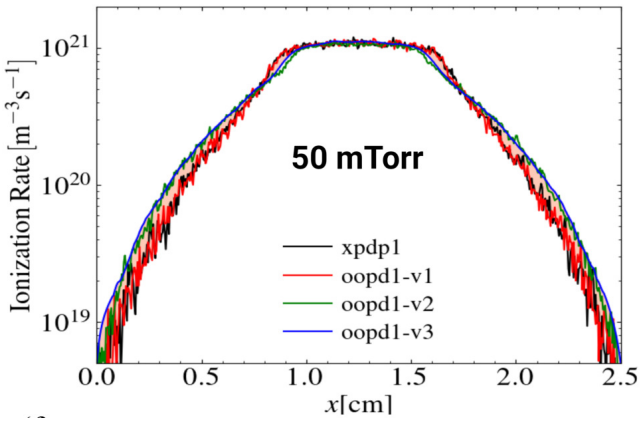

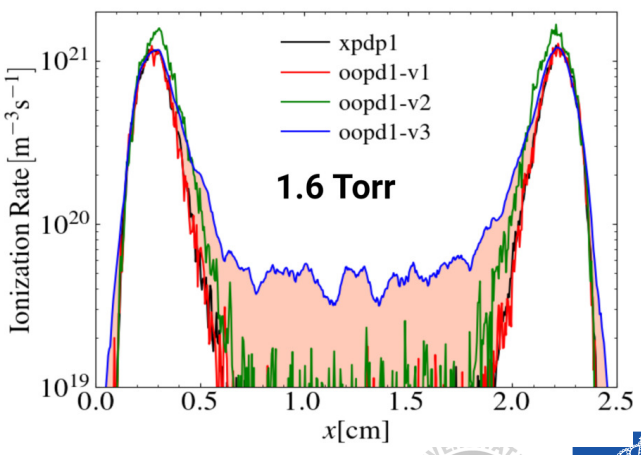

Wen et al. (2021) PSST **30** 105009

Pressure dependence

- The time averaged ion density profile for various pressures calculated
  - without excited state atoms (upper)
  - including excited state atoms treated as a fluid (lower)
  - rf current source at 50 $\mathrm{A/m^2}$ and 13.56 MHz
- The metastable $\mathrm{Ar^m}$, the radiative $\mathrm{Ar^r}$, and the Ar(4p) manifold are included and modeled as time- and space-evolving fluid species
- It is found that the presence of the excited species influences the density profile and enhances the plasma density by a factor of 3 at 1.6 Torr

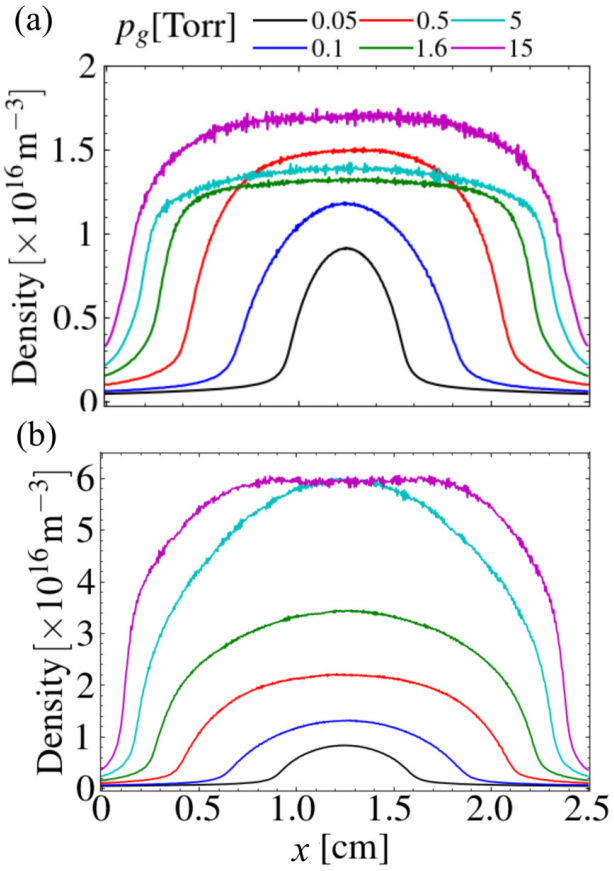

Wen et al. (2022) IEEE TPS **50**(9) 2548

Pressure dependence

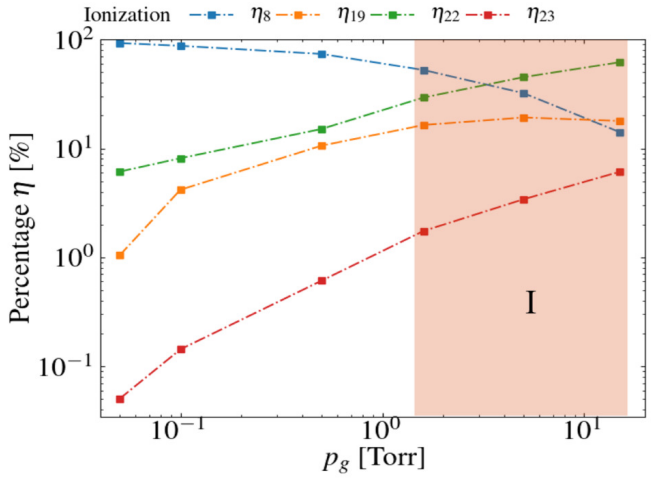

Wen et al. (2021) PSST **30** 105009

- Percentage (η_j) of the total reaction rate of each reaction *j* versus background pressure p_g
  Ionization
  - R8: $e^- + Ar \rightarrow 2e^- + Ar^+$ dominates at low pressure
  - R22: $Ar^m + Ar^m \rightarrow e^- + Ar^+ + Ar$ – Penning ionization and
  - R19: $e^- + Ar^m \rightarrow e^- + Ar^+ + Ar$ – step wise ionization take over at higher pressure

Surface effects – secondary electron emission

Surface effects

Table 2. The parameters of the simulation, the energy threshold above which the PIC dynamics of the neutral particles are followed, the wall quenching and reflection coefficients, and secondary electron emission yield upon particle impact.

Species	$\mathcal{E}_{thr}$ (mV)	γ_q	γ_r	γ_{see}
Ar	1000		1.0	$f(\mathcal{E}_n)$ [46, 47]
Ar^m	50	0.5	0.5 [45]	0.21 [48]
Ar^r	50	0.5	0.5 [45]	0.21 [48]
Ar(4p)	50	0.5	0.5 [45]	0.27 [48]
Ar^+		—	—	$f(\mathcal{E}_i)$ [46, 47]
e		—	0.2 [49]	—

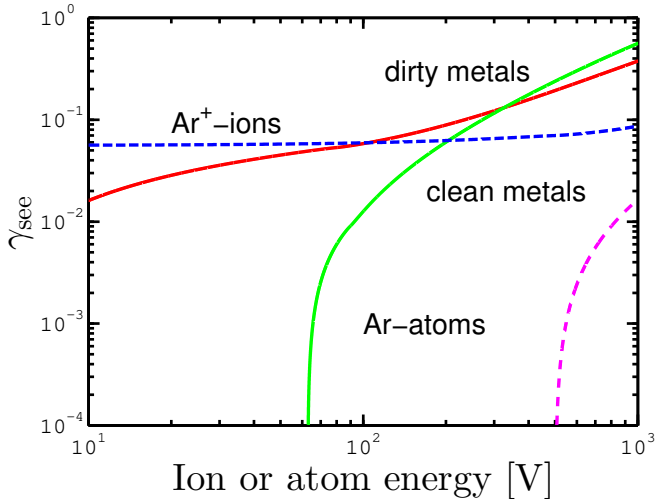

Gudmundsson et al. (2021) PSST **30** 125011

based on Phelps and Petrović (1999) PSST **8** R21

- Secondary electron emission
  - Ion induced, energy dependent
  - Due to bombardment of neutrals in the ground state
  - Due to bombardment of excited neutrals

Secondary electron emission

Secondary electron emission due to

- Electron bombardment of the electrodes
  - Using the modified Vaughan method as described by Wen et al. (2023)
- Photon bombardment of the electrodes
- The resonance radiation of Ar^r is partially imprisoned at low pressure, and the fraction of the radiation escaping depends on the specific gas pressure and electrode spacing
- We use the Walsh model to calculate the escape factor *g*

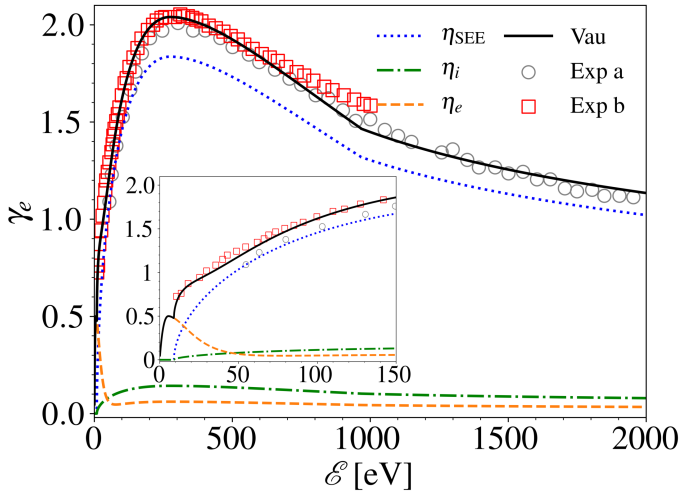

Wen et al. (2023) PSST **32** 064001

Secondary electron emission

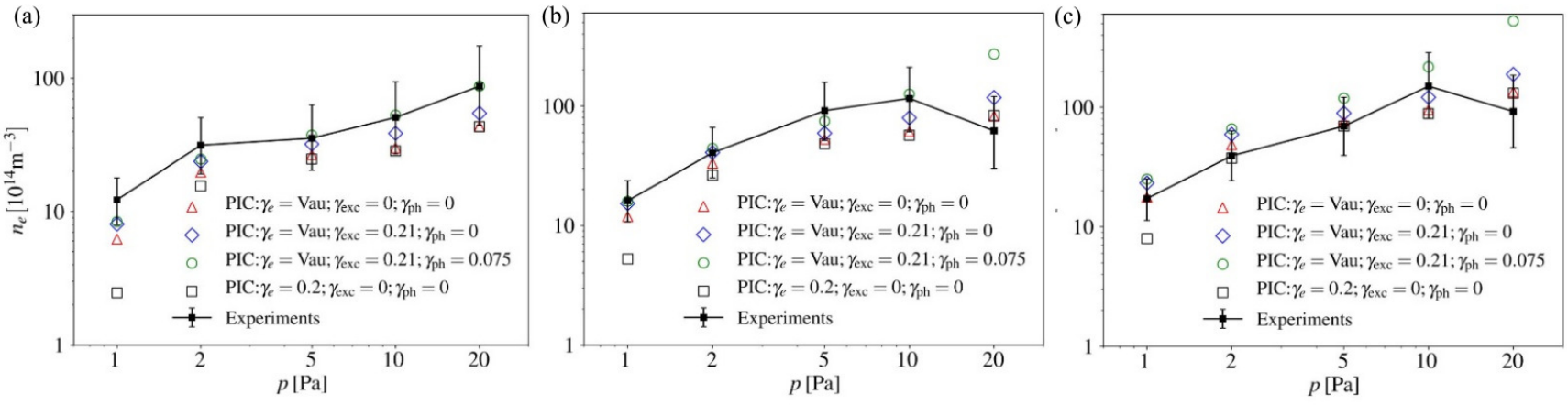

Wen et al. (2023) PSST **32** 064001

- The figures show the electron density versus gas pressure for three driving voltage amplitudes
- The figures show the PIC/MCC simulation results for varying completness of the surface processes
- The black dotted lines the experimental measurements of the plasma density at the discharge center by Schulenberg et al.

Schulenberg et al. (2021) PSST **30**(10) 105003

Summary


UNIVERSITATIS ISLANDIAE
SIGILLUM


KTH
VETENSKAP
OCH KONST

Summary

- The particle-in-cell Monte Carlo collsion simulations are a very important tool to explore processes in low-temperature plasma discharges
- An overview of verifaction methods for 1D particle-in-cell Monte Carlo collision simulation codes
- This includes
  - **Verification**: A comparison of simulations and analytical solutions to test the intrinsic consistency of a model
  - **Validation**: A comparison of simulations with experimental results or observations
  - **Benchmarking**: A comparison of two or more models under the same conditions, but with different numerical implementations or on different scales (like particle or fluid models)
- We looked at code verification using analytical verification solution and the method of manufactured solutions (MMS)

Thank you for your attention

tumi@hi.is

The slides can be downloaded at

http://langmuir.raunvis.hi.is/~tumi/ranns.html

References

Godyak, V. A. and R. B. Piejak (1990). Abnormally low electron energy and heating-mode transition in a low-pressure argon rf discharge at 13.56 MHz. *Physical Review Letters 65*(8), 996–999.

Gudmundsson, J. T., E. Kawamura, and M. A. Lieberman (2013). A benchmark study of a capacitively coupled oxygen discharge of the oopd1 particle-in-cell Monte Carlo code. *Plasma Sources Science and Technology 22*(3), 035011.

Gudmundsson, J. T. and M. A. Lieberman (2015). On the role of metastables in capacitively coupled oxygen discharges. *Plasma Sources Science and Technology 24*(3), 035016.

Gudmundsson, J. T., J. Krek, D.-Q. Wen, E. Kawamura, and M. A. Lieberman (2021). Surface effects in a capacitive argon discharge in the intermediate pressure regime. *Plasma Sources Science and Technology 30*(12), 125011.

Kim, H. C., O. Manuilenko, and J. K. Lee (2005). Particle-in-cell Monte-Carlo simulation of capacitive RF discharges: Comparison with experimental data. *Japanese Journal of Applied Physics 44*(4A), 1957–1958.

Lafleur, T. (2020). Space-charge limited current with a finite injection velocity revisited. *Plasma Sources Science and Technology 29*(6), 065002.

Lafleur, T. (2022). Space-charge affected current flow: an analytical verification solution for kinetic and fluid simulation models. *Plasma Sources Science and Technology 31*(11), 114008.

Lafleur, T., P. Chabert, and J. P. Booth (2014). Electron heating in capacitively coupled plasmas revisited. *Plasma Sources Science and Technology 23*(3), 035010.

Oberkampf, W. L. and C. J. Roy (2010). *Verification and Validation in Scientific Computing*. Cambridge, United Kingdom: Cambridge University Press.

Phelps, A. V. and Z. L. Petrović (1999). Cold-cathode discharges and breakdown in argon: surface and gas phase production of secondary electrons. *Plasma Sources Science and Technology 8*(3), R21–R44.

Riva, F., C. F. Beadle, and P. Ricci (2017). A methodology for the rigorous verification of particle-in-cell simulations. *Physics of Plasmas 24*(5), 055703.

Schulenberg, D. A., I. Korolov, Z. Donkó, A. Derzsi, and J. Schulze (2021). Multi-diagnostic experimental validation of 1d3v PIC/MCC simulations of low pressure capacitive RF plasmas operated in argon. *Plasma Sources Science and Technology 30*(10), 105003.

References

Surendra, M. (1995). Radiofrequency discharge benchmark model comparison. *Plasma Sources Science and Technology 4*(1), 56–73.

Tranquilli, P., L. Ricketson, and L. Chacón (2022). A deterministic verification strategy for electrostatic particle-in-cell algorithms in arbitrary spatial dimensions using the method of manufactured solutions. *Journal of Computational Physics 448*, 110751.

Turner, M. M., A. Derzsi, Z. Donkó, D. Eremin, S. J. Kelly, T. Lafleur, and T. Mussenbrock (2013). Simulation benchmarks for low-pressure plasmas: Capacitive discharges. *Physics of Plasmas 20*(1), 013507.

Vahedi, V., C. K. Birdsall, M. A. Lieberman, G. DiPeso, and T. D. Rognlien (1993). Capacitive rf discharges modelled by particle-in-cell Monte Carlo simulation. II. Comparisons with laboratory measurements of electron energy distribution functions. *Plasma Sources Science and Technology 2*(4), 273–278.

Wen, D.-Q., J. Krek, J. T. Gudmundsson, E. Kawamura, M. A. Lieberman, and J. P. Verboncoeur (2021). Benchmarked and upgraded particle-in-cell simulations of capacitive argon dischargeat intermediate pressure: The role of metastable atoms. *Plasma Sources Science and Technology 30*(10), 105009.

Wen, D.-Q., J. Krek, J. T. Gudmundsson, E. Kawamura, M. A. Lieberman, P. Zhang, and J. P. Verboncoeur (2023). On the importance of excited state species in low pressure capacitively coupled plasma argon discharges. *Plasma Sources Science and Technology 32*(6), 064001.

Wen, D.-Q., J. Krek, J. T. Gudmundsson, E. Kamamura, M. A. Lieberman, and J. P. Verboncoeur (2022). Particle-in-cell simulations with fluid metastable atoms in capacitive argon discharges: electron elastic scattering and plasma density profile transition. *IEEE Transactions on Plasma Science 50*(9), 2548–2557.

Wen, D.-Q., J. Krek, J. T. Gudmundsson, E. Kawamura, M. A. Lieberman, and J. P. Verboncoeur (2021). Benchmarked and upgraded particle-in-cell simulations of capacitive argon dischargeat intermediate pressure: The role of metastable atoms. *Plasma Sources Science and Technology 30*(10), 105009.

Wen, D.-Q., J. Krek, J. T. Gudmundsson, E. Kawamura, M. A. Lieberman, P. Zhang, and J. P. Verboncoeur (2023). On the importance of excited state species in low pressure capacitively coupled plasma argon discharges. *Plasma Sources Science and Technology 32*(6), 064001.